HITTITE JOURNAL OF SCIENCE AND ENGINEERING

e-ISSN: 2148-4171
Volume: 11 • Number: 4
December 2024

Evaluating the Combined Effects of Transverse Pitch Ratio and Flow Arrangement on the Thermo-Hydraulic Performance of a Novel Inclined Delta Winglet

Hüseyin Zahit Demirağ
Yozgat Bozok University, Department of Mechanical Engineering, 66200, Yozgat, Türkiye.

Corresponding Author

Hüseyin Zahit Demirağ
E-mail: zahit.demirag@bozok.edu.tr Phone: +90354 242 1001
RORID: https://ror.org/04qvdf239

Article Information

Article Type: Research Article
Doi: https://doi.org/10.17350/HJSE19030000344
Received: 13.09.2024
Accepted: 07.11.2024
Published: 31.12.2024

Cite As

Demirağ H, Z. Evaluating the Combined Effects of Transverse Pitch Ratio and Flow Arrangement on the Thermo-Hydraulic Performance of a Novel Inclined Delta Winglet. Hittite J Sci Eng. 2024;11(4):169-180.

Peer Review: Evaluated by independent reviewers working in at least two different institutions appointed by the field editor.
Ethical Statement: Not available.
Plagiarism Checks: Yes - iThenticate
Conflict of Interest: Author approves that to the best of their knowledge, there is not any conflict of interest or common interest with an institution/organization or a person that may affect the review process of the paper.

CRediT AUTHOR STATEMENT
Hüseyin Zahit Demirağ: Conceptualization, Data curation, Formal Analysis, Investigation, Methodology, Resources, Supervision, Writing – review and editing.

Evaluating the Combined Effects of Transverse Pitch Ratio and Flow Arrangement on the Thermo-Hydraulic Performance of a Novel Inclined Delta Winglet

Hüseyin Zahit Demirağ

Yozgat Bozok University, Department of Mechanical Engineering, 66200, Yozgat, Türkiye.

Abstract

In this work, the in-depth examinations of the Novel Inclined Delta Winglet (NIDW) in terms of heat transfer performance and the flow characteristics are conducted at Re=5000-17500, utilizing (SST) k-ω turbulence model. In accordance with the objective of this investigation, the combined effects of the positioning of the NIDW in common-flow-down (NIDW-CFlowD) and common-flow-up (NIDW-CFlowU) orientations together with two transverse pitch ratios [P_t=0.333 and 0.166] are investigated and the resulting data are presented in a comparative manner. The angle of attack [α=30°] and the angle of inclination [β=30°] of the NIDW are kept constant. The numerical results indicate that the NIDW-CFlowD orientation at P_t=0.333 has more pronounced effect in terms of thermal performance, with an approximate increase of 4.29% increase in the Nusselt number at Re=17500, whereas the opposite trend is observed at P_t=0.166, yielding a smaller rise of around 3.13% in Nusselt number at Re=17500. The reversal in trend is entirely due to the positioning of the NIDW in the CFlowD orientation, which causes the vortex rotation centers to move further apart in the main flow direction, resulting in 4.36% and 4.02% higher Darcy friction factors in cases of P_t=0.333 and P_t=0.166, respectively compared to CFlowU configuration at Re=5000. Therefore, the highest and lowest ranges of Thermal Enhancement Factor (TEF) are calculated to be between 1.325-1.215 and 1.221-1.122 for the cases of NIDW-CFlowU with P_t=0.166 and NIDW-CFlowU with P_t=0.333 respectively. This corresponds to an increase in TEF of around 8.52%and 8.30% increase in TEF at Re=5000 and 17000, respectively.

Keywords: Novel inclined delta winglet, common-flow-up/down orientations, turbulent flow, transverse pitch ratio, thermo-hydraulic performance

INTRODUCTION

Solar Air Heater (SAH) is a one of the widely utilized [1][2][3] a type of heat exchanger that is particularly suited to low-temperature applications. They are preferred due to a number of factors, including their low capital and operating costs, simple configuration, ease of maintenance, being eco-friendly [4] and etc. A SAH is designed with the objective of maximizing the transfer of absorbed solar energy to the moving air [5], and thus ensuring the highest possible level of convective heat transfer between the absorber plate and the air. However, given the fact that the air's convective heat transfer coefficient is relatively poor [6][7], leading to the resistance to heat flow at considerable level [8][9][10]. To overcome this phenomenon, one of the most effective methods is to place a Vortex Generator (VG) heated surface of heat exchangers where the heat transfer takes place [11][12]. In this regard, two of the primary parameters, investigated in the method of enhancing convective heat transfer through the utilization of VG, encompass the positioning of the VG in different flow orientations including common-flow-up/down and the transverse pitch ratios.

In a configuration in which the distance between the leading edges of vortex generators in a plane perpendicular to the main flow is either greater or smaller than that between the trailing edges, the resulting flow structures are referred to as common-flow-up and common-flow-down, respectively. Despite the lack of explicit preference for either flow pattern in the existing literature with regard to thermal performance, the vortex interactions with the boundary layer exhibit notable differences between common-flow-up and common-flow-down orientations.

Accordingly, in order to investigate the impacts of flow patterns on thermal performance, Ke et al. [13] carried out numerical analysis to investigate the effect of delta winglet vortex generators on heat transfer and Darcy friction factor in a rectangular channel. Based on their numerical resulting data, they concluded that the common-flow-up configuration showed improved effectiveness when the delta winglet aspect ratio was relatively low, while the common-flow-down layout showed superior performance when the aspect ratio was high. Kim and Yang [14] performed detailed experimental investigation in order to study the flow characteristics and heat transfer performance of counter-rotating vortices. The boundary layer interaction becomes stronger than the vortex interaction as the longitudinal vortex pair in the common-flow-down moves downstream. However, the vortex interaction is stronger than the boundary layer interaction in the case of the longitudinal vortex pair in the common-flow-up flow pattern. Therefore, they emphasized that the common-flow-down configurations have better heat transfer characteristics than the cases with the common-flow-up orientation. Tian et al. [15] conducted a numerical study with the aim of comparing the thermal performance of DWP and RWP positioned on the bottom surface of the duct in common-flow-up/down configurations under a fixed angle of attack of β = 45°. They stated that DWP-inserted channel showed a comparable overall performance for common-flow-down and common-flow-up configurations, whereas, in the case of RWP-inserted channel, common-flow-down orientation offer superior overall performance compared to the common-flow-up flow pattern. In a numerical study, Salleh et al. [16] emphasized that VGs generate a high momentum rotating flow in the 'wake region', defined as the low pressure region under the common-flow-down configuration. On the other hand, they stated that VGs act like a nozzle under the common-flow-up orientation, increasing the flow velocity and delaying the flow separation behind the pipe, and improvements are obtained in these regions where heat transfer is low. In their research, Fu et al. [17] investigated the impact of common-flow-up/down flow configurations, as well as their arrangement either at the same or opposite channel walls, in terms of the heat transfer and friction factor characteristics of a minichannel within the Reynolds number range of 3000-18000. The researchers observed that in the common-flow-up-1 configuration, the two vortices formed behind the LVGs, occupy the majority of the channel, resulting in a uniform distribution of velocity and that the vortex-occupied areas exhibit higher velocity. In contrast, the primary vortex in the common-flow-down-1 configuration occupies a larger area. However, the core of the channel exhibits enhanced velocity and a thinner thermal boundary layer in the vicinity of the bottom wall.

Another parameter investigated to increase the TEF is the ratio of the transverse spacing between the VGs to channel width, which is generally denoted as the transverse pitch ratio [P_t] when VGs are positioned along the channel width. In particular, in the case of insufficient transverse spacing between VGs, negative interaction between the velocity components of the vortices in the plane perpendicular to the flow direction causes the turbulence intensity to decrease and Darcy friction factor to be elevated as well. It is therefore of great importance to determine the optimum values of all these dimensionless parameters in order to achieve the highest possible level of convection heat transfer by increasing the turbulence intensity throughout the test region, while achieving the lowest possible pressure drop.

Within this framework, Song et al. [18] carried out computational assessment, focusing on the significance of the transverse pitch ratio with respect to pressure drop characteristics and heat transfer performance. They emphasized that the interaction between longitudinal vortices leads to a reduction in vortex intensity with a higher pressure drop along test region. They concluded that the increases in vortex intensity and Nusselt number of up to 21.4% and 29.2%, respectively, at optimum pitch. Tanaka et al. [19] carried out both numerical and experimental assessment with an objective of determining optimum parameters within the range of Re=360-3600. Their results suggest that an optimum transverse pitch, S_t, is attained at S_t/H_d=3 (or greater), which effectively prevents the interaction of vortices by adjacent rectangular winglets. Dogan and Erzincan [20] also highlighted the fact that one of the key parameters in terms of thermal performance is the transverse pitch ratio, and the optimum transverse pitch ratio for attaining the highest TEF is determined to be R_T = 0.16. Skullong and Promvonge [21] also examined the influence of two transverse pitches of R_P = 1 and 2 on heat transfer and friction factor characteristics, spanning the range of Re=5000-24000. They determined that the greatest value of TEF is achieved through the incorporation of DWs at R_P = 1. Hu et al. [22] carried out experimental study regarding the impact of one-eighth sphere vortex generators (OES-VGs) on heat transfer and friction factor performance in the range of Re=4000-19000. They pointed out that a reduction in the S/H ratio allows for the installation of a greater number of OES-VGs on the absorber within the same duct length, resulting in an increase in fluid disturbances, which amplifies the turbulence of the air surrounding the absorber plate, thereby enhancing the convective transfer of heat. Furthermore, Demirağ H.Z. [23] also pointed out that a reduction in the transverse pitch ratio, resulting in an increased number of NIDWs in a single row, is the main factor contributing to the elevated Nusselt number (or Nu/Nu_0 ratio). This is due to the fact that the doubling of the NIDWs, which leads to the formation of twice as many longitudinal vortices within the fluid domain test region, consequently amplifies the impact on the heated surface.

A review of existing literature reveals that studies have been predominantly examined the effects of transverse pitch ratio and the impacts of CFlowU or CFlowD flow patterns on thermal performance independently. To the best of our knowledge, no previous studies have explored the combined impacts of these two variables, despite the presence of significant distinctions in longitudinal vortex interactions and vortex center spacing in the cases of CFlowU and CFlowD flow patterns, which have a substantial potential to affect thermo-hydraulic performance. Accordingly, this study provides a unique analysis distinct from previous research [23] by examining the combined impacts of two different transverse pitch ratios and CFlowU and CFlowD flow patterns on the thermo-hydraulic performance of NIDW at Re=5000-17500. This approach not only provides a new dimension to understanding the thermal performance of NIDW but also addresses an important gap by examining the interplay between these two variables in a unified context.

MATERIAL AND METHODS

A comprehensive description of the numerical model employed in this study is presented in this section. This part also provides information regarding the validation of the model and the computational methods utilized.

Computational Model Details

The computational domain for NIDW-fitted duct is constituted by three parts, including the computational domain inlet, exit and test regions. The computational domain inlet and exit regions lengths are determined by considering the dimensions of smooth duct computational domain identified at previous work [23]. In this context, the inlet and the exit region lengths are set to L_{Inlet}= 1000 mm and L_{Exit}= 500 mm, respectively. Moreover, the channel geometry measurements from the prior numerical analysis [23] also provided a basis for determinations of the test region's height [H=30 mm], length [L_{Test}=440 mm] and width [W=300 mm], respectively. Furthermore, the dimensions of the NIDW, utilized in this numerical assessment, is presented in Figure 1. The inclination angle, angle of attack, slant angle, base-attached edge length and height of NIDW are donated as α, β, θ, k and b, respectively.

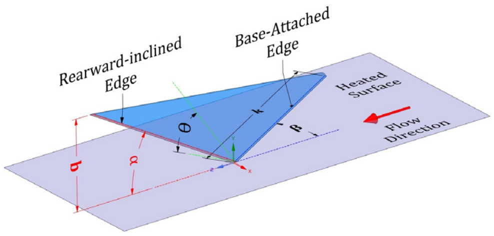

Figure 1 The dimensional definitions and isometric view of NIDW [23]

In this numerical work, detailed computational investigations are conducted on the impacts of the NIDW's transverse pitch ratio, P_t, together with its orientations, including CFlowU and CFlowD, regarding thermal performance and Darcy friction factor in the range of Re=5000-17500. It should be emphasized that, as in the previous study [23], the frontal projection areas in the plane perpendicular to the main flow are kept constant throughout all cases investigated in this work. However, unlike in the preceding research [23], the NIDW's geometry are not scaled. On the contrary, to ensure equal frontal projection areas for NIDW-CFlowU and NIDW-CFlowD cases with P_t=0.333 , the geometric dimensions are set to b=15 mm and k=30 mm for NIDW-CFlowU and NIDW-CFlowD cases at P_t=0.166, as depicted in Figure 2. Due to fact that the highest TEF values are achieved using NIDW with α=30° and β=30°in the previous work [23], the attack [β=30°] and inclination [α=30°] angles are also remained fixed in this work. Lastly, in this numerical assessment, the NIDW-CFlowU case with P_t=0.333 is considered the reference case.

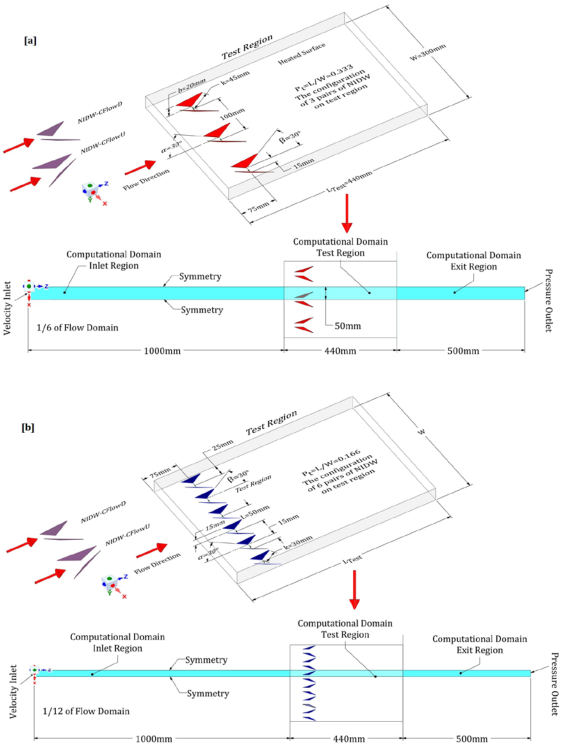

Figure 2 Geometric configurations and boundary conditions of computational domains of NIDW-CFlowD at a) P_t=0.333 and b) P_t=0.166

As illustrated in Figure 2, due to the implementation of symmetry boundary conditions within the computational fluid domain, the cases of NIDW-CFlowU or NIDW-CFlowD-fitted ducts at $P_t = L_{NIDW}/W$ [transverse spacing between two pairs of NIDW/channel width] =0.333 and 0.166, the computational domain accounts for 1/6 and 1/12 of the total flow domain, respectively. The upper wall of the rectangular duct within the test region has been designated as the heated surface on which the uniform heat flux [$q''=600W/m^2$] applied.

Mesh Structure

The performing of the mesh independence test is of great significance, not only in regard to the saving of computational resources and the reduction of time required, but also with respect to the assurance of the validity of the resulting numerical data. It should be noted, however, that, the data for the reference case of NIDW-CFlowU with P_t=0.333 [α=30° and β=30°] as well as the smooth duct data are sourced from prior work [23]. The reference case of NIDW-CFlowU with P_t=0.333 utilized grid parameters derived from a grid independence test carried out in a previous study [23]. Accordingly, a distinct mesh independence test is not conducted in the present study. Instead, the mesh structures of all cases analyzed in this numerical assessment, are generated with consideration of the mesh parameters established for the reference case. The grid structure of NIDW-CFlowD at P_t=0.333 is presented in Figure 3. As is seen in Figure 3, the mesh structure consists of a subdivision of the computational domain into different volumes, with the number of cells in the computational domain test region being greater than both the inlet and outlet of computational domains. In addition, the flow volume encapsulating the NIDW-CFlowD has a denser mesh structure than neighboring volumes in the test region. The aim of this approach is the accurate calculation of velocity and temperature gradients. For an accurate computation of the velocity gradients, the number of cells is also concentrated at the edges and corners of NIDW-CFlowD, at which the flow separates. In addition, more than 10 inflation layers are identified in all cases investigated. Furthermore, the first layer height is set to 0.05 mm and 0.025 mm for the smooth and NIDW-equipped channels, respectively. In conclusion, growth rate is set to 1.15.

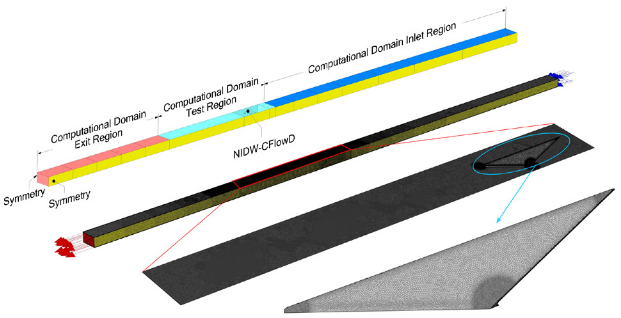

Figure 3 The computational domain grid structure consists of 8667708 polyhedral cells for the NIDW-CFlowD at P_t=0.333

Numerical Method and Data Analysis

ANSYS Fluent Computational Fluid Dynamics (CFD) software is utilized to perform numerical analysis, and the governing equations are discretized using the finite volume approach. The convective terms are discretized with a second-order upwind approach, and the Coupled algorithm handles the pressure-velocity coupling. A three-dimensional flow simulation is conducted given the assumptions of steady state, incompressible turbulent flow, with viscous dissipation effects being excluded. More information on the numerical method and boundary conditions applied in the numerical assessment are given in previous computational study [23]. Furthermore, the numerical analysis of both the smooth and NIDW-fitted channels are performed with the utilization of non-dimensional numbers of Nusselt number (Nu), Reynolds number (Re), Darcy friction factor (*f*) and TEF. Further details regarding non-dimensional numbers utilized in this study is detailed in previous work [23].

Governing Equations and Turbulence Model

The numerical examination of the turbulent airflow in a rectangular duct is carried out utilizing the RANS equations. The relevant formulas of energy, momentum and continuity based on the conditions of incompressible flow and constant thermophysical parameters are given as:

Equation of Continuity

$$\frac{\partial}{\partial x_i}(\rho u_i) = 0$$

Equation of Momentum

$$\frac{\partial}{\partial x_j}(\rho u_i u_j) = -\frac{\partial P}{\partial x_i} + \frac{\partial}{\partial x_j}\left[\mu\left(\frac{\partial u_i}{\partial x_j} - \rho\overline{u_i' u_j'}\right)\right]$$

The Reynolds stress term, $-\rho u_i' u_j'$ is detailed in Eq.-3 through the use of the Boussinesq approximation

$$-\rho\overline{u_i' u_j'} = \mu_t\left(\frac{\partial u_i}{\partial x_j} + \frac{\partial u_j}{\partial x_i}\right) - \frac{2}{3}\left(\rho k + \mu_t\frac{\partial u_i}{\partial x_i}\right)\delta_{ij}$$

Equation of Energy

$$\frac{\partial}{\partial x_i}[u_i(\rho E + P)] = \frac{\partial}{\partial x_j}\left[\left(k + \frac{C_p \mu_t}{Pr_t}\right)\frac{\partial T}{\partial x_j} + u_i(\tau_{ij})_{eff}\right.$$

$$(\tau_{ij})_{eff} = \mu_{eff}\left(\frac{\partial u_j}{\partial x_i} + \frac{\partial u_i}{\partial x_j}\right) - \frac{2}{3}\mu_{eff}\frac{\partial u_k}{\partial x_k}\delta$$

where, $(\tau_{ij})_{eff}$, c_p and k are represented by the following: energy stress tensor, specific heat capacity and thermal conductivity.

Additionally, the (SST) k-ω turbulence model is utilized because of its proven proficiency to analyze separated flows, adverse pressure gradients, and boundary layers, effectively. An adaptation of the k–ω turbulence model [24] by Menter [25], which is the (SST) k-ω turbulence model specifics are available in prior numerical assessment [23].

The Assessment of Validation Study

In general terms, the performance of a turbulence model is tested by performing simulations of chaotic flow conditions, including swirling flow, flow re-attachment, flow separation and heat transfer analysis. Accordingly, in this first part of validation study, the Nusselt number and Darcy friction factors of the experimental work, possibly involving the above-mentioned flow conditions, are verified by employing the (SST) k-ω turbulence model. The details regarding experimental configuration and boundary conditions for the computational domain are illustrated in Figure 4, whereas Figure 5 presents the numerical Nusselt numbers (Nu) and Darcy friction factors (*f*) in comparison with the data derived from the experimental correlation equations. In the context of the experimental setup of DW-E at R_p=2, α=45° and *b/H*=0.5 [21], the computational analysis yields mean absolute deviation rates of 1.18% and 1.14% for Nu and *f*, respectively, in comparison to the experimental correlation data. The suitability of the (SST) k-ω turbulence model for further investigations is confirmed by the close agreement between the data sets. It is also important to note that in the previous numerical assessment, the smooth channel Darcy friction factor (f_0) and Nusselt number (Nu_0) are verified by comparison with the Petukhov and Dittus-Boelter correlation equations, respectively [23].

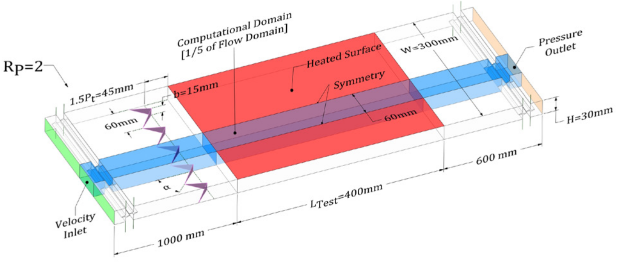

Figure 4 The visual illustration of experimental setup and the corresponding boundary conditions regarding to the computational domain (denoted in blue) for DW-E at R_p=2, α=45° and *b/H*=0.5

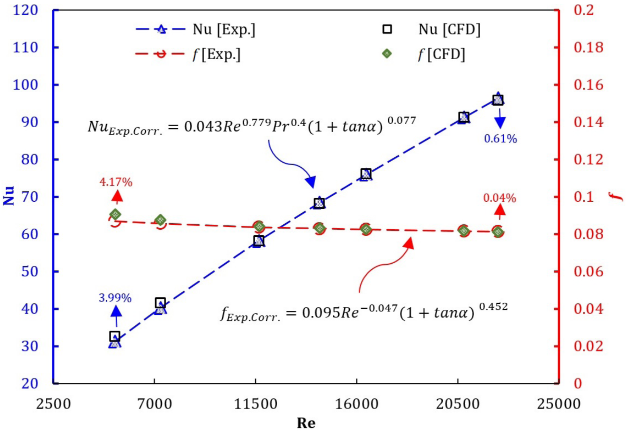

Figure 5 The verification of DW-E at R_p=2, α=45° and *b/H*=0.5 with an experimental correlation data

Furthermore, in the second part, the objective is to provide additional evidence to demonstrate the performance of the (SST) k-ω turbulence model. In this regard, the validation study is also carried out in local manner at Re=15000. Accordingly, local Nu_x/Nu_0 ratio of inline 60° V-discrete ribs are verified for *z/D*=1/4 at Re=15000. The numerical setup of inline 60° V-discrete ribs [26][27] and the corresponding boundary condition for the computational domain (1/4 of periodic module) are illustrated in Figure 6.

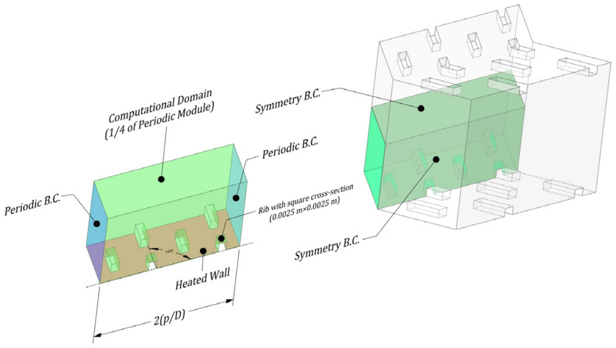

Figure 6 The visual representation of inline 60° V-discrete ribs and the corresponding boundary conditions regarding to the periodic computational domain (denoted in yellow) [26][27]

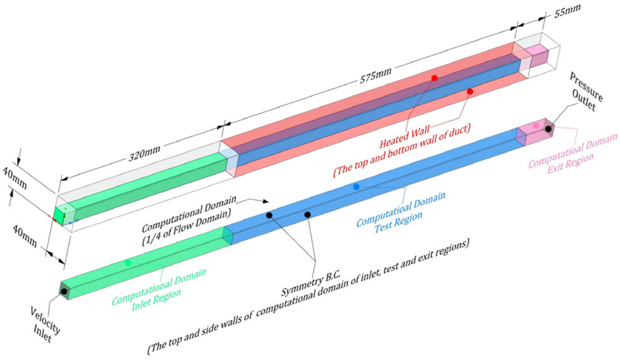

Figure 7 The schematic representation of smooth channel with a square cross-section and the corresponding boundary conditions regarding to the computational domain [27]

Additionally, smooth channel validation study is also undertaken at Re=15000 to calculate Nu_x/Nu_0 ratio at z/D=1/4. The schematic representation of the smooth duct, together with the corresponding boundary conditions for its computational domain, is shown in Figure 7.

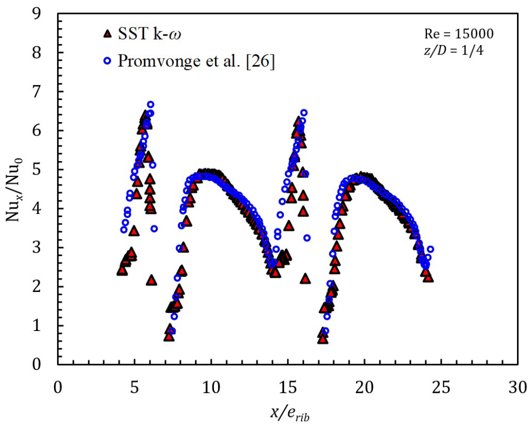

Figure 8 The verification of local Nux/Nu0 ratios for z/D=1/4 at Re=15000

The resulting numerical data indicate that the deviation rate for Nu_0 and f_0 with respect to the Dittus-Boelter and Petukhov correlation equations is 0.82% and 9.65%, respectively. Notably, the local Nu_x/Nu_0 ratios demonstrate excellent agreement with the numerical data from the study conducted by Promvonge et al. [26], as illustrated in Figure 8.

RESULTS AND DISCUSSIONS

This section presents a comprehensive investigation focusing into the influence of NIDW in different orientations, including CFlowD and CFlowU configurations at P_t=0.333 and P_t=0.166, on convective heat transfer performance and friction factor characteristics. In this section, all data for the smooth channel and NIDW-CFlowU at P_t=0.333 cases are sourced from the prior study [23].

Heat Transfer

The Nusselt number change of the positioning of NIDW in different orientations at P_t=0.333 and P_t=0.166 across the range of Reynolds numbers from 5000 to 17500 is given in the Figure 9-a, b, c, d. In a manner analogous to the behavior observed in smooth duct, the Nusselt number demonstrates a progressive increase as the Reynolds number is elevated. The underlying mechanism behind this phenomenon can be attributed to the intensified velocities of turbulent eddies, which increase interaction with the thermal boundary layer and thereby enhance convective heat transfer. The motion of eddies through the fluid results in the disruption of the boundary layer. This occurs as a consequence of the exchange of fluid in different temperatures, with the cooler core fluid mixing with the warmer fluid at the surface. The resulting increase in thermal resistance close to the wall is reduced by this process of enhanced mixing, resulting in a greater overall heat transfer rate within the system. The augmentation in convective heat transfer yields an elevated Nusselt number. It can therefore be concluded that in all cases examined, the maximum Nusselt numbers are achieved at the highest Reynolds number investigated. Furthermore, the insertion of NIDWs at diverse orientations and transverse pitch ratios into channel's flow domain has been observed to result in an elevated Nusselt number in comparison to the case of smooth channel at Re=5000-17500.

The longitudinal vortices produced by the NIDW [Figure 10], contribute to the enhancement of Nusselt number by being effective along the test region. This is because a swirling flow pattern disrupts the orderly movement of the fluid and increases the chaotic nature of the fluid, which further increases the rate of mixing of low and high temperature fluids.

Furthermore, vortices elevate the local velocity of the fluid in the vicinity of the heated surface, which inhibits the expansion of the thermal boundary layer on heated surface. Therefore, in comparison to the smooth channel case, there is a notable reduction in the area-weighted average static temperature of heated surface, providing a definitive indication of the rise in Nusselt number for NIDW-CFlowU and NIDW-CFlowD at P_t=0.333 and P_t=0.166, as demonstrated in Figure 11.

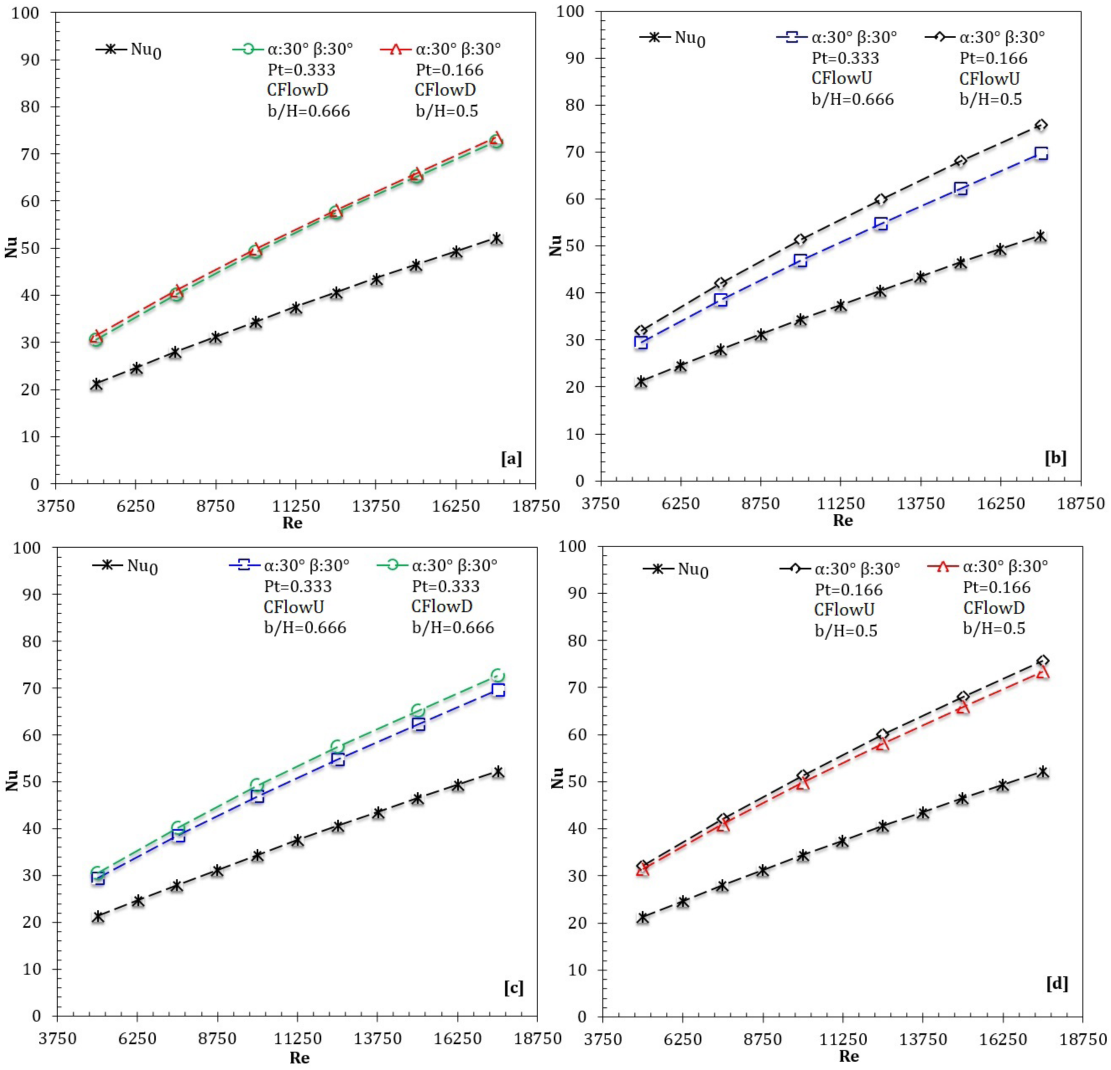

Figure 9 The variation of Nu number for a) NIDW-CFlowD at P_t=0.333 and P_t=0.166 b) NIDW-CFlowU at P_t=0.333 and P_t=0.166 c) NIDW-CFlowD and NIDW-CFlowU at P_t=0.333 d) NIDW-CFlowD and NIDW-CFlowU at P_t=0.166

Moreover, the time-averaged contour maps of the static temperature variation in conjunction with the local Nusselt number distribution demonstrate that the lowest static temperature and the corresponding highest local surface Nusselt number are observed at the trailing end of the vortex generator besides the entrance of the heated surface in all cases examined. The formation of the strongest vortices right behind the NIDW, and the subsequent gradual weakening of the vortices in the direction of the main flow as a result of viscous forces, provide a clear explanation for this situation. Nevertheless, even at the endpoint of the test region, they still continue to exert an influence on the growth of the thermal boundary. However, when comparing the effects of positioning the NIDW in different orientations and transverse pitch ratios on thermal behavior, a significant difference is observed in each cases.

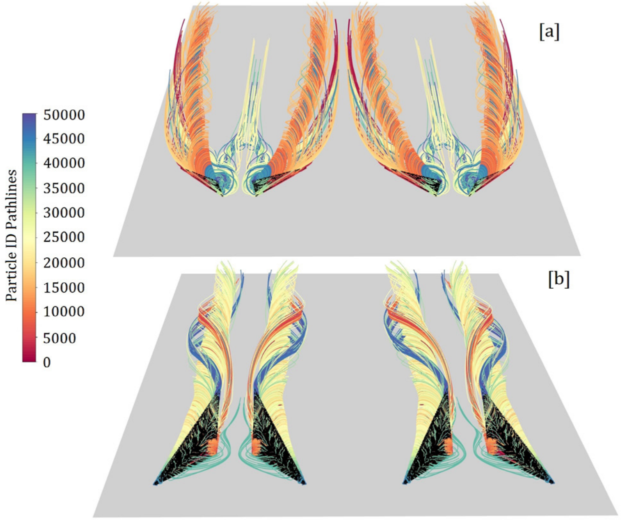

Figure 10 The 3D representation of longitudinal vortices produced by a) NIDW-CFlowD and b) NIDW-CFlowU at Re=17500

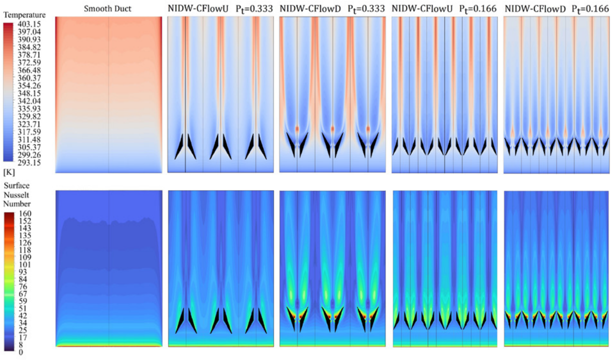

Figure 11 The time-averaged contour maps of static temperature and local Nu number variations of heated surface for both smooth duct and NIDW-fitted duct, including CFlowU and CFlowD arrangements for P_t=0.333 and 0.166 at Re=5000

With regard to the impact of transverse pitch ratio on convective heat transfer performance, the highest Nusselt numbers are observed within the range of Re=5000-17500 for P_t=0.166 and P_t=0.333, respectively when NIDW is positioned in either CFlowU or CFlowD orientations as plotted in Figure 9-a and Figure 9-b. This is attributed to the presence of a double number of longitudinal vortices along the heated surface in the case of P_t=0.166 compared to the transverse pitch ratio of P_t=0.333. The closer spacing between NIDWs in the case of P_t=0.166 results in intensified vortex-thermal boundary layer interactions, which disrupt the growth of thermal boundary layer more vigorously. This, in turn, enhances turbulent mixing high-and low-temperature fluid zones in flow domain, leading to reduced thermal resistance and resulting in an increased Nusselt number in comparison to the transverse pitch ratio of P_t=0.333. However, when NIDW is positioned in the CFlowD orientation, the increase in Nusselt number is negligibly small at P_t=0.166 in comparison to the transverse pitch ratio of P_t=0.333 (Figure 9-a) and thus, similar Nusselt numbers are obtained in the range of Re=5000-25000. Conversely, the elevation in Nusselt numbers are significantly higher at P_t=0.166 than at P_t=0.333 when NIDW is in the CFlowU pattern as given in Figure 9-b. The observed rise in Nusselt number is predominantly attributable to the longitudinal vortices generated by NIDW-CFlowD, whose rotation centers exhibit a tendency to spread farther apart in the direction of the mainstream, as illustrated in Figure 10 and Figure 12. This phenomenon lessens the influence of vortices on the heated surface along the flow direction while increasing their contact with one another. Therefore, while vortices are found to be effective right behind NIDW in both the CFlowU and CFlowD arrangements (Figure 11), their impact on heated surface in the CFlowD configuration is less pronounced than it is in the CFlowU configuration at P_t=0.166. Accordingly, for NIDW in the CFlowU configuration at P_t=0.166, lower temperature values are obtained over a significantly larger area of the heated surface than NIDW-CFlowD, as depicted in Figure 11, and thus higher Nusselt numbers are obtained spanning Reynolds number between 5000 and 17500, as plotted in Figure 9-d. Moreover, by examining the time-averaged streamline velocity distributions at six planes perpendicular to the main flow, dimensionless distance [$P=x/L$] ranging from P1 = 0.25 to P6 = 0.875, within the computational domain test region, it was determined that in the CFlowD pattern, a tendency of vortex centers to spread apart in the direction of the main flow has a noticeable adverse impact on thermal performance, when P_t=0.166. In contrast to the CFlowU arrangement, this tendency caused the vortex centers to drift away from the heating surface, where NIDW is situated (Figure 12), and thus negatively affecting the enhancement of convective heat transfer.

However, an opposing trend has been noted in the instance of P_t=0.333 as presented in Figure 9-c. As illustrated in Figure 12, the vortices generated by the CFlowD pattern exert a considerable shear stress near the heated surface with the centers of the main vortices positioned much nearer to the heated wall along the test region in comparison to the CFlowU orientation, thereby promoting enhanced cross-sectional mixing and intensifying thermal boundary interaction, which leads to higher convective heat transfer at P_t=0.333. Additionally, although the separation of the eddies' centers in the main flow direction causes interaction between the vortices to be increased, as previously stated, the positioning of the NIDW in the CFlowD configuration at P_t=0.333 allows for the formation of additional secondary vortices between the two main vortices as depicted in Figure 10. This is because the spacing between the vortices is not small enough as in the case of P_t=0.166, to significantly influence one another negatively. This phenomenon provides an explanation for the attainment of higher Nusselt numbers, particularly just behind the NIDW-CFlowD at P_t=0.333, as depicted in Figure 11.

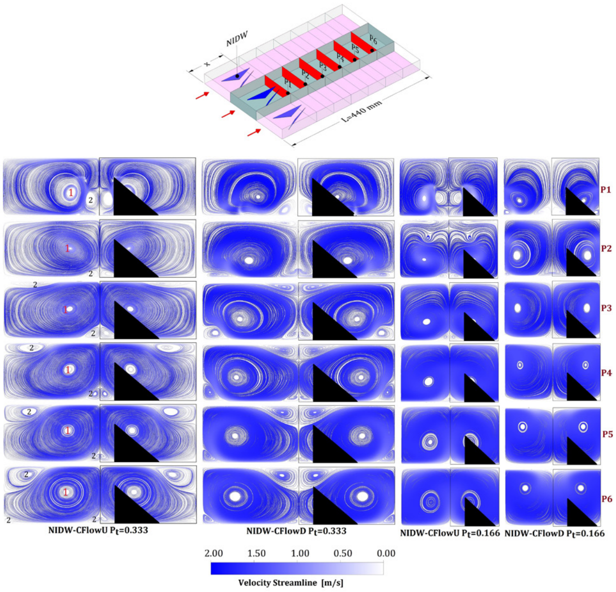

Figure 12 The time-averaged streamline velocity distribution at P1=0.25, P2=0.375, P3=0.5, P4=0.625, P5=0.75 and P6=0.875 for NIDWs in CFlowU and CFlowD orientations at P_t=0.333 and 0.166 at Re=5000

Friction Factor

The Darcy friction factor, *f*, changes in NIDW positioning in different orientations at two different transverse pitch ratios together with the smooth channel Darcy friction factors are

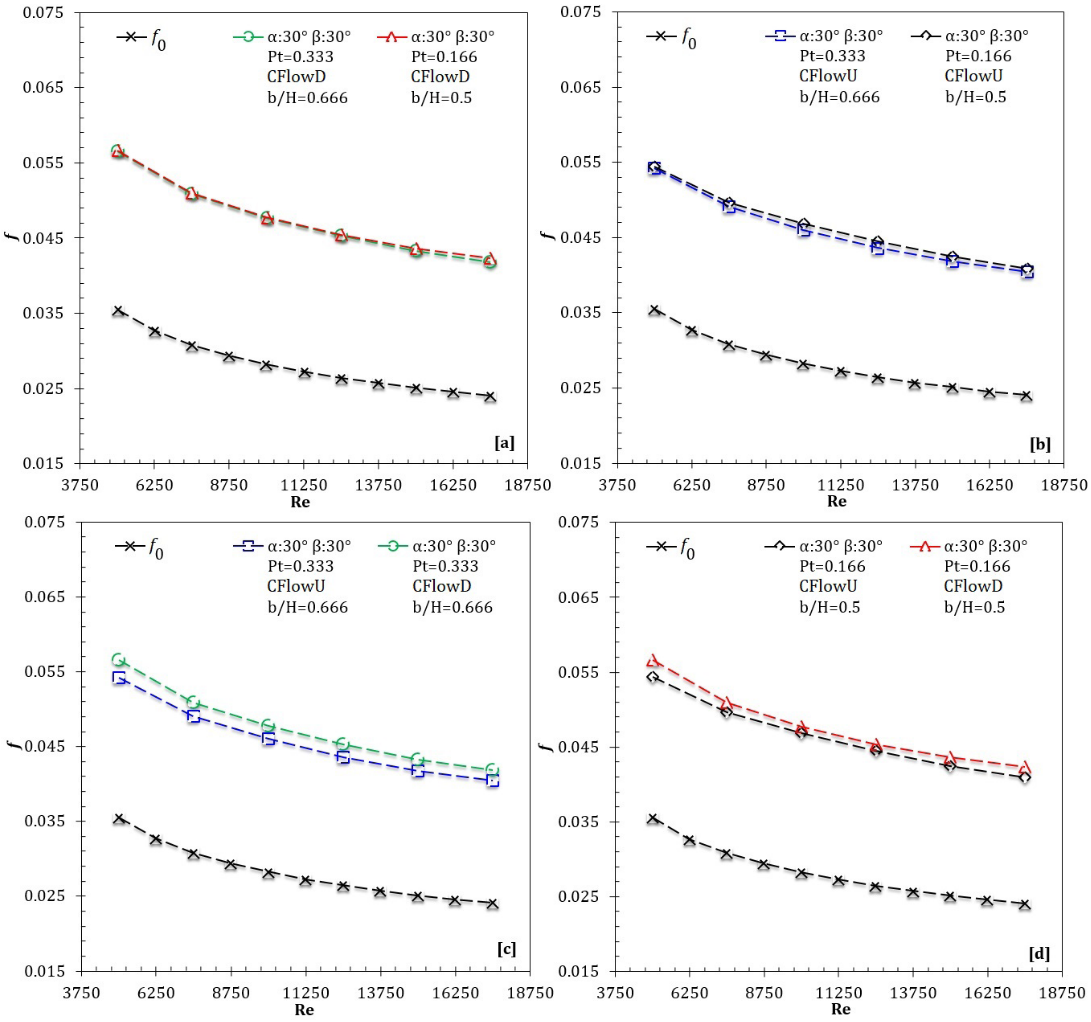

Figure 13 The variation of f for a) NIDW-CFlowD at P_t=0.333 and P_t=0.166 b) NIDW-CFlowU at P_t=0.333 and P_t=0.166 c) NIDW-CFlowD and NIDW-CFlowU at P_t=0.333 d) NIDW-CFlowD and NIDW-CFlowU at P_t=0.166

In the present study, the effects of the transverse pitch ratio and the impacts of the configurations of CFlowU and CFlowD, are considered independently of the frontal projected area. Consequently, the frontal projected areas normal to the main stream are held constant in each case examined. Accordingly, the aforementioned factors, which exert a relatively minor influence on the rise in pressure loss across the test region, play an effective role in the rise in the friction factor as plotted Figure 13-c, and Figure 13-d. As previously stated, a comparison of the CFlowU and CFlowD orientations at each case of P_t=0.166 or P_t=0.333 reveals that despite both having an equal total frontal projection areas, there are notable differences in the resulting Darcy friction factors. The CFlowD configurations of NIDW are calculated to attain higher Darcy friction factor values covering the Reynolds number range from 5000 to 17500 for both transverse pitch ratios, as plotted in Figure 13-c, and Figure 13-d. The underlying reason of this phenomenon can be attributed to the tendency of vortex centers to diverge in the direction of the main flow when the NIDW is positioned in CFlowD configuration. In order to provide a visual illustration of the resulting data, the Q-criterion based vortex structures are presented for each cases, investigated, comparatively in Figure 14. As illustrated in Figure 14, the notable interaction between the vortices is evidently apparent for the NIDW-CFlowD, positioning under a transverse pitch ratio of P_t=0.166, resulting in the highest Darcy friction factor in the range Re=5000-17500.

Another significant finding is that the presence of a double number of longitudinal vortices in the case of P_t=0.166 results in higher Darcy friction factor for NIDW-CFlowD and NIDW-CFlowU-fitted channels at Re=5000-17500 as plotted in Figure 13-a, and Figure 13-b, respectively. In other words, the increase in the number of longitudinal vortices in a single row intensifies eddy interactions within each channel, thereby enhancing turbulence and disrupting the boundary layer in the vicinity of the channel walls to a greater extent. This disruption results in an increased momentum exchange between the vortices and the channel wall, which in turn raises the drag and consequently yields higher flow resistance. As a result, the channels fitted with NIDW-CFlowU and NIDW-CFlowD at P_t=0.166 exhibit higher Darcy friction factors compared to those at P_t=0.333.

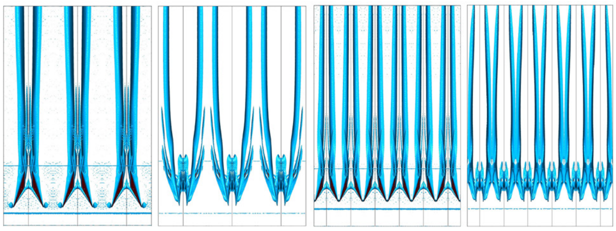
NIDW-CFlowU P_t=0.333 NIDW-CFlowD P_t=0.333 NIDW-CFlowU P_t=0.166 NIDW-CFlowD P_t=0.166

Figure 14 The comparison of vortex structures illustrated by Q-criterion

THERMAL ENHANCEMENT FACTOR

The changes in TEF for NIDWs mounted in rectangular channel in various flow patterns, including CFlowU and CFlowD configurations and transverse pitch ratios, are presented in a comparable way in Figure 15-a, b, c, d. In all cases examined, including NIDW-CFlowD at P_t=0.166 and P_t=0.333 and the NIDW-CFlowU at P_t=0.166 and P_t=0.333, a decreasing trend in the TEF values are obtained with a rise in Reynolds number, ranging from 5000 to 17500. Furthermore, the TEF values for both CFlowD and CFlowU flow patterns in the Re=5000–17500 range, are calculated to be higher at P_t=0.166 than at P_t=0.333 as shown in Figure 15-a and Figure 15-b, respectively. This is due to the increase in the number of longitudinal vortices along test region, leading to a larger increase in convective heat transfer in comparison to the rise in friction factor. Moreover, the rise in TEF values is even more pronounced in CFlowU flow pattern in comparison to CFlowD configuration (Figure 15-b) due to previously mentioned factor of which is the divergence tendency of vortices in the mainstream direction.

However, when the effects of different flow patterns on TEF at constant transverse pitch ratios are examined comparatively, CFlowU flow pattern is more favorable in case of P_t=0.166 (Figure 15-d), whereas there is an opposite trend in case of P_t=0.333 (Figure 15-c) is present and thus, higher TEF values are obtained when NIDW is positioned in CFlowD orientation at P_t=0.333 within the range of Re=5000-17500. As a result, the TEF values obtained by positioning NIDW-CFlowU and NIDW-CFlowD in the rectangular channel at P_t=0.333 and P_t=0.166 at Re = 5000 - 17500 are calculated to be between 1.221-1.122 and 1.325-1.215 (CFlowU); 1.244-1.157 and 1.279-1.165 (CFlowD), respectively. Accordingly, the highest TEF value of 1.325 is achieved with an insertion of NIDW-CFlowU at P_t=0.166 and Re=5000.

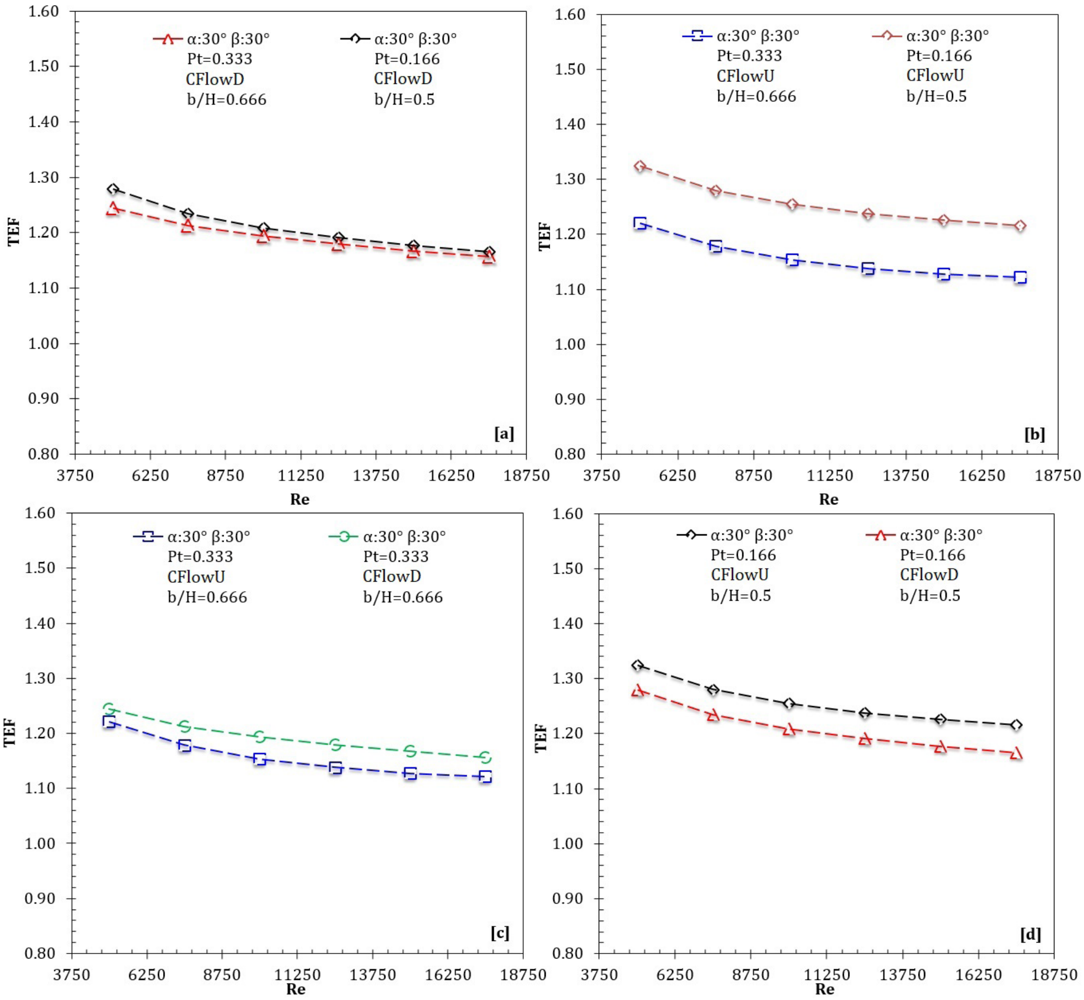

Figure 15 The variation of TEF for a) NIDW-CFlowD at P_t=0.333 and P_t=0.166 b) NIDW-CFlowU at P_t=0.333 and P_t=0.166 c) NIDW-CFlowD and NIDW-CFlowU at P_t=0.333 d) NIDW-CFlowD and NIDW-CFlowU at P_t=0.166

CONCLUSION

This computational examination focuses on the influence of orientation-based factors, encompassing CFlowU and CFlowD flow patterns and transverse pitch ratios of P_t=0.166 and P_t=0.333, regarding thermal performance and flow behaviors at Re=5000-17500. In numerical analysis, both the angle of attack [β=30°] and the angle of inclination [α=30°] are kept constant. Various combinations with the same frontal projection areas of the NIDW are investigated in terms of thermo-hydraulic performance in detail in a comparative manner.

The following represents a summary of the conclusions:

- The configurations of CFlowU and CFlowD along with the transverse pitch ratio have notable influence on the enhancement of heat transfer performance and flow characteristics as well. Although the presence of the double number of longitudinal vortices has a significant impact on the increase of both the Nusselt number and the Darcy friction factor, the orientation of the NIDW plays a key role. Thus, the highest Darcy friction factor and Nusselt number are obtained with the insertion of NIDW-CFlowD and NIDW-CFlowU at P_t=0.166.
- The distance between the vortex centers within the flow volume exhibited no discernible change in the CFlowU configuration as a result of arranging the NIDWs in various transverse pitch ratios. Nonetheless, at P_t=0.166 and P_t=0.333, it was noted that the centers of vortices in the CFlowD setup became increasingly farther apart in the main flow direction. Additionally, the tendency forced centers of vortices to shift away from the heated surface as well at P_t=0.166.
- The CFlowD configuration at P_t=0.166 has a negative effect on the heat transfer performance due to the tendency of the vortices to diverge in the direction of the main flow. However, the distance between the NIDWS at P_t=0.333 is sufficient to trigger the formation of secondary vortices along with the main vortices, resulting in the higher Nusselt numbers being achieved.
- The maximum and minimum TEF values are achieved between 1.325 - 1.215 and 1.221 - 1.122 for the cases of NIDW-CFlowU with P_t=0.166 and NIDW-CFlowU with P_t=0.333, respectively.

Acknowledgment

The author received no financial support for the research of this article.

References

1. Goel V, Hans VS, Singh S, Kumar R, Pathak SK, Singla M, et al. A comprehensive study on the progressive development and applications of solar air heaters. Sol Energy 2021. https://doi.org/10.1016/j.solener.2021.07.040.
2. Yadav AS, Mishra A, Dwivedi K, Agrawal A, Galphat A, Sharma N. Investigation on performance enhancement due to rib roughened solar air heater. Mater Today Proc 2022. https://doi.org/10.1016/j.matpr.2022.05.071.
3. Ghritlahre HK, Sahu PK, Chand S. Thermal performance and heat transfer analysis of arc shaped roughened solar air heater – An experimental study. Sol Energy 2020. https://doi.org/10.1016/j.solener.2020.01.068.
4. Ahirwar B kumar, kumar A. Review on different techniques used to enhance the thermal performance of solar air heater. Int J Heat Mass Transf 2024. https://doi.org/10.1016/j.ijheatmasstransfer.2023.124979.
5. Chompookham T, Eiamsa–ard S, Buanak K, Promvonge P, Maruyama N, Hirota M, et al. Thermal performance augmentation in a solar air heater with twisted multiple V–baffles. Int J Therm Sci 2024;205:109295. https://doi.org/10.1016/j.ijthermalsci.2024.109295.
6. Kumar R, Chand P. Performance enhancement of solar air heater using herringbone corrugated fins. Energy 2017. https://doi.org/10.1016/j.energy.2017.03.128.
7. Saravanan A, Murugan M, Reddy MS, Ranjit PS, Elumalai P V., Kumar P, et al. Thermo-hydraulic performance of a solar air heater with staggered C-shape finned absorber plate. Int J Therm Sci 2021. https://doi.org/10.1016/j.ijthermalsci.2021.107068.
8. Biswas G, Chattopadhyay H, Sinha A. Augmentation of heat transfer by creation of streamwise longitudinal vortices using vortex generators. Heat Transf Eng 2012. https://doi.org/10.1080/01457632.2012.614150.
9. He J, Liu L, Jacobi AM. Air-side heat-transfer enhancement by a new winglet-type vortex generator array in a plain-fin round-tube heat exchanger. J Heat Transfer 2010. https://doi.org/10.1115/1.4000988.
10. Chang LM, Wang LB, Song KW, Sun DL, Fan JF. Numerical study of the relationship between heat transfer enhancement and absolute vorticity flux along main flow direction in a channel formed by a flat tube bank fin with vortex generators. Int J Heat Mass Transf 2009. https://doi.org/10.1016/j.ijheatmasstransfer.2008.09.029.
11. Min C, Qi C, Kong X, Dong J. Experimental study of rectangular channel with modified rectangular longitudinal vortex generators. Int J Heat Mass Transf 2010. https://doi.org/10.1016/j.ijheatmasstransfer.2010.03.026.
12. Xu Z, Han Z, Wang J, Liu Z. The characteristics of heat transfer and flow resistance in a rectangular channel with vortex generators. Int J Heat Mass Transf 2018. https://doi.org/10.1016/j.ijheatmasstransfer.2017.08.083.
13. Ke Z, Chen CL, Li K, Wang S, Chen CH. Vortex dynamics and heat transfer of longitudinal vortex generators in a rectangular channel. Int J Heat Mass Transf 2019. https://doi.org/10.1016/j.ijheatmasstransfer.2018.12.064.
14. Kim E, Yang JS. An experimental study of heat transfer characteristics of a pair of longitudinal vortices using color capturing technique. Int J Heat Mass Transf 2002. https://doi.org/10.1016/S0017-9310(02)00054-6.
15. Tian LT, He YL, Lei YG, Tao WQ. Numerical study of fluid flow and heat transfer in a flat-plate channel with longitudinal vortex generators by applying field synergy principle analysis. Int Commun Heat Mass Transf 2009. https://doi.org/10.1016/j.icheatmasstransfer.2008.10.018.
16. Md Salleh MF, Gholami A, Wahid MA. Numerical evaluation of thermal hydraulic performance in fin-and-tube heat exchangers with various vortex generator geometries arranged in common-flow-down or common-flow-up. J Heat Transfer 2019;141. https://doi.org/10.1115/1.4041832.
17. Fu H, Sun H, Yang L, Yan L, Luan Y, Magagnato F. Effects of the configuration of the delta winglet longitudinal vortex generators and channel height on flow and heat transfer in

minichannels. Appl Therm Eng 2023. https://doi.org/10.1016/j.applthermaleng.2023.120401.

18. Song KW, Wang L, Hu YJ, Liu Q. Flow symmetry and heat transfer characteristics of winglet vortex generators arranged in common flow up configuration. Symmetry (Basel) 2020. https://doi.org/10.3390/sym12020247.
19. Tanaka T, Itoh M, Hatada T, Matsushima H. Influence of inclination angle, attack angle, and arrangement of rectangular vortex generators on heat transfer performance. Heat Transf - Asian Res 2003. https://doi.org/10.1002/htj.10089.
20. Dogan M, Erzincan S. Experimental investigation of thermal performance of novel type vortex generator in rectangular channel. Int Commun Heat Mass Transf 2023. https://doi.org/10.1016/j.icheatmasstransfer.2023.106785.
21. Skullong S, Promvonge P. Experimental investigation on turbulent convection in solar air heater channel fitted with delta winglet vortex generator. Chinese J Chem Eng 2014. https://doi.org/10.1016/S1004-9541(14)60030-6.
22. Hu J, Zhang Y, Xie S, Xiao Y. Thermo-hydraulic performance of solar air heater with built-in one-eighth sphere vortex generators. Appl Therm Eng 2024. https://doi.org/10.1016/j.applthermaleng.2024.122837.
23. Demirağ HZ. Innovative approach for longitudinal vortex generator design: Impact on thermal performance. Therm Sci Eng Prog 2024. https://doi.org/10.1016/j.tsep.2024.102444.
24. Wilcox DC. Turbulence Modeling for CFD (Third Edition). DCW Ind 2006.
25. Menter FR. Two-equation eddy-viscosity turbulence models for engineering applications. AIAA J 1994. https://doi.org/10.2514/3.12149.
26. Promvonge P, Changcharoen W, Kwankaomeng S, Thianpong C. Numerical heat transfer study of turbulent square-duct flow through inline V-shaped discrete ribs. Int Commun Heat Mass Transf 2011. https://doi.org/10.1016/j.icheatmasstransfer.2011.07.014.
27. SriHarsha V, Prabhu S V., Vedula RP. Influence of rib height on the local heat transfer distribution and pressure drop in a square channel with 90° continuous and 60° V-broken ribs. Appl Therm Eng 2009. https://doi.org/10.1016/j.applthermaleng.2008.12.015.